Effect of Different Wall Materials in Thermoelectric Electricity Production

Diogo Manuel Gervásio de Almeida
diogo.gervasio.almeida@tecnico.ulisboa.pt

Instituto Superior Técnico, Universidade de Lisboa, Portugal

October 2021

Abstract

The use of clay as the combustor wall material for direct heat-to-electricity conversion using a Thermoelectric generator (TEG) was evaluated in a side-wall configuration burner. The influence of different fuel blends (Methane, Biogas and Biogas + H_2) and flame work conditions in TEG power and efficiency are discussed. A galvanized steel plate was use for comparison with the clay results. A mathematical model was developed to predict electrical power generated for different fuel, flame conditions, wall materials and thicknesses, using the finite element method and experimental results obtained. The gases velocity field was studied with Particle Image Velocimetry (PIV). It was found that the efficiency and electrical power losses between materials increases with flame temperature.

Keywords: thermoelectric generator, clay, flame-wall interaction, heat transfer, chemiluminescence

1. Introduction

In recent decades, the awareness for climate changes has grown. In 2015, the Paris Agreement was signed by 197 countries, representing almost the total greenhouse gas emission worldwide, in a joint effort to limit the temperature rise to under 2 ℃, ideally below 1.5 ℃, above the pre-industrial levels.

Energy demands are expected to continue to increase in the next few decades, following the predicted growth in world population and industry. Although the share of renewable sources in electricity production is projected to increase, fossil fuels will still play an important role over the coming years.

At the same time, there is still a vast number of people who live in decentralized rural areas, not connected to the grid, that do not have access to electricity. The solution commonly adopted by governments and aid agencies is the construction of mini grids powered by solar photovoltaic panels and batteries, that provide electricity to the village. In this situation, providing a minimum amount of electricity, *e.g.* for lighting, can make a substantial difference.

To power LED lights or charge equipment, thermoelectric generators (TEG) are one of the alternative solutions to solar power in rural electrification. TEG offer great reliability, silent and on-demand electricity source, instantly converting the heat from flames, furnaces or boilers into electricity [1]. The TEG is normally encapsulated between a metallic wall and a heat sink. However, stoves in these locations are usually made of the available materials, namely stone and clay.

Biomass anaerobic digestion is a biological decomposition process which transforms organic matter, that if disposed without any treatment would be harmful to the environment, *e.g.* soil and water contamination, into biogas (BG) and inorganic substances. The use of biogas helps cutback on fossil fuel usage and reduces greenhouse gas emissions. However, the weak combustion properties of biogas restrict its range of applications. The blending of small amounts of hydrogen (H_2) with biogas enables its direct use in burners without the need for upgrading or purification. The injection of small quantities of H_2 represents an intermediate phase in the growth of hydrogen technology.

2. Experimental Setup

2.1. Equipment and setup

A lamella burner with two slits (length $l_s = 40$ mm and width $w_s = 2$ mm, each) and a stainless steel flame holder were used to acquire a laminar V-shape flame. One branch of the flame interacts with a vertical wall, positioned 1.5 mm above the burner and 2 mm away from the flame holder. Connected to the wall is a thermoelectric generator, which extracts heat from the hot wall to produce electricity. An adapted CPU heat exchanger (Phanteks Glacier C350i) is placed on the other side of the TEG to draw the excessive heat out and maintain the temperatures on the cold side of the TEG as low as possible. The TEG used is a commercially available GM200-49-45-30 from European Thermodynamics. The wall is slightly raised above the burner in order to maximized the area for heat transfer, but not enough for the unburnt mixture to escape underneath. This position is maintained throughout all experiments. The wall is used to protect the TEG from direct contact with the flame and from exceeding the maximum temperature advised by the manufacturer. Information about the TEG module can be found in Table 1.

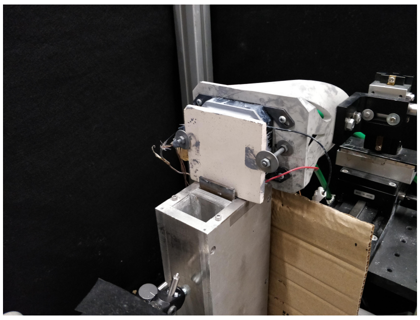

Figure 1: Pictures of the experimental setup perspective view.

Table 1: GM200-49-45-30 thermoelectric datasheet characteristics

Dimensions	$62 \times 62 \times 5.8mm$
Maximum Temperature	$T_{H,max} = 200^{\circ}$
	$T_{C,max} = 175^{\circ}$
Performance for:	$T_H = 200^{\circ}$
	$T_C = 30^{\circ}$
Matched load output power	7.5 W
Matched load resistance	$0.28\ \Omega \pm 15\%$
Open circuit voltage	2.8 V
Heat flow through module	$\approx 149W$

A galvanized steel (GS) plate, henceforth designated by wall, ($90 \times 75 \times 1$ mm, $\kappa_{wall} = 56.7$ W/mK [5]) and a clay wall were used ($80 \times 80 \times 6.5$ mm, $\kappa_{wall} = 1.3$ W/mK [5]).

Tap water is supplied to the HX and its flow rate is monitored with a Bailey Fischer Porter D10A1197D flow meter (148 l/h capacity). The water enters at the bottom and exits, after passing through a series of fins, at the top of the HX. The wall and the HX are fixed to a 3D printed support. The TEG is hold in place by compression. To reduce thermal contact resistances and improve heat conduction, thermal paste (AG Termopasty HPX, $\kappa = 2.8$ W/mk) is applied to all TEG, wall, and HX surfaces in contact.

The different fuels blends are obtained by combining CH_4, CO_2 and H_2, drawn from gas bottles (Air liquid Alphagaz 99.95%). Dried compressed air is used to achieve the desired equivalence ratios. Alicat Scientific M-series mass flow meters were used to controlled each mixture flow rate. The flow meters have a maximum capacity of 5, 5, 1 and 50 SLPM, respectively, and their set points are controlled with an in-house developed program with LabView software. The gases are mixed in a small chamber, which then connects to the burner via a single tube.

2.1.1 Power and temperature acquisitions

Six OMEGA k-type thermocouples and a Data Translation DT9828 acquisition board are used to acquired the TEG surfaces and water temperatures. Two thermocouples are placed on each side of the TEG, separated by 30 mm in the y direction (Figure 2a). At the inlet and outlet of the HX, a thermocouple is inserted into the water tube, as close as possible to the HX. The acquisition board is connected to a computer, where the readings are monitored, and recorded, using the QuickDAQ software.

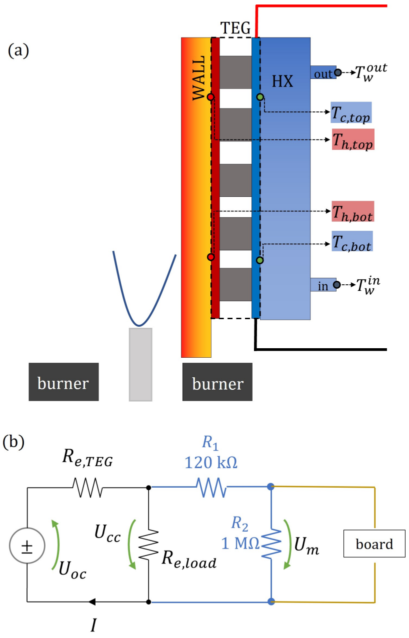

Figure 2: Scheme of (a) thermocouple position and (b) electrical circuit.

The TEG terminals are connected to an electrical load, made of ceramic resistances, and a circuit divider, which divides the closed circuit voltage (U_{cc}) by nearly 10 times and enables the monitoring of the voltage U_m with the acquisition board. A scheme of the electrical circuit connected to the TEG terminals is illustrated in Figure 2b. The circuit divider is needed because the board can only handle voltages up to 312 mV, but the TEG open circuit voltage

(U_{oc}) can reach up to 3V. The load resistance used is $R_{e,load} = 0.281\,\Omega$.

2.1.2 PIV

Aluminium oxide (Al_2O_3) particles, with diameter $d = 1\mu$m, were used as seeding particles. Their chemical inactivity and high melting point ($T \approx 2350$ K) makes then appropriate for studying combustion reactive flows. The particles were agitated in a flask, with the help of a magnetic stirrer, and carried with the unburnt mixture. The particle density was controlled by regulating the rotational speed of the magnetic stirrer.

The Dantec DualPower 65-15 Nd:YAG laser was used to illuminate the Al_2O_3 particles. The laser has two beams, which emit light with a wavelength of 532 nm. After passing through a lens, it produces a light sheet with a thickness of $t_s \approx 1$ mm. The light sheets were adjusted to overlay at the burner exit. Each light pulse lasts for 4ns.

A Nikon 60 mm f/2.8D lens was assembled to An ANDOR Zyla 5.5 sCMOS camera to capture particle images. The camera operated in double-frame acquisition. The laser and the camera were connected to a BNC Model 575 synchronizer. The camera and the synchronizer were also connected to the computer. Exposure times, number of images, repetition rate and post processing were controlled using the Dantec DynamicStudio v5.1 software [2].

For acquisitions of the reactive flow (with the flame) a 532 nm CVI Melles Griot light bandpass filter (3nm bandwidth) was placed in front of the lens. The filter is only permeable for the light reflected from the particles, blocking the light emitted by the flame in other wavelengths.

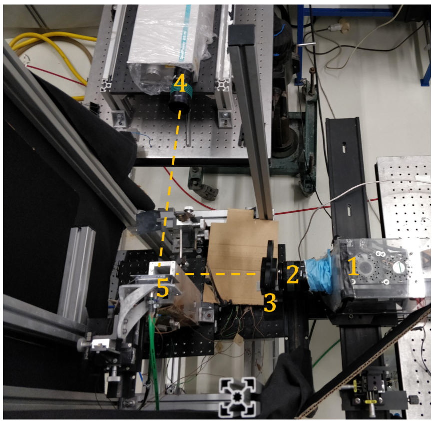

Figure 3: PIV experimental setup with (1) camera, (2) lens, (3) 532 nm optical filter, (4) laser and (5) main setup shown in Figure 1.

2.2. Experimental procedure

For all analysis, different fuel blends were used: pure methane (BG100) and two blends of biogas (BG80 and BG60). The number after "BG" denotes the amount of CH_4 in the biogas blend (BG80 represents a blend of biogas with 80% CH_4 and 20% CO_2, and BG60 a blend with 60% CH_4 and 40% CO_2). Hydrogen is added to BG60 and BG80 blends in a 10% and 20% volume percentage. The fuel blends are named BG**X** + **Y**% H_2, where **X** is the volumetric percentage of CH_4 in biogas and **Y** is the volumetric percentage of H_2. The molar fraction of each species in the mixture can be calculated from:

$$\chi_{H_2} = \mathbf{Y}/100 \tag{1}$$

$$\chi_{CH_4} = \mathbf{X}(1 - \chi_{H_2}) \tag{2}$$

$$\chi_{CO_2} = 1 - \chi_{H_2} - \chi_{CH_4} \tag{3}$$

The set point for each gas flow meter depends on the burner Reynolds number (Re) and the mixture equivalence ratio (ϕ). Re was calculated based on the unburnt mixture properties with a characteristic dimension equal to the burner slit width ($w_s = 2$ mm):

$$Re = \frac{\dot{V}_u}{2 \times \nu_u \times l_s} \tag{4}$$

where $\dot{V}_u$ [m^3/s], ρ_u [kg/m^3], μ_u [Ns/m^2] and ν [m^2/s] are the unburnt mixture volumetric flow rate, density, and, dynamic and kinetic viscosity, respectively, and $l_s = 40$ mm is the burner slit length. The Reynolds number studied range from 100 to 350. The equivalence ratios tested ranged 0.7 to 1.0. The water flow rate was set to 1.23 LPM, which corresponds to 50% of the flow meter's maximum capacity.

A room temperature of $T_u = 298.15$ K and atmospheric pressure were assumed at the exit of the burner when computing the volumetric flow rate at STP conditions for the set points of the flow meters, using the ideal gas law $p = \rho_u R_0 T$. The flame power (P_{flm}) was calculated from the mixture low heating value (LHV [J/kg]), ρ_u and fuel mass fraction (Y_F):

$$P_{flm} = \mathrm{LHV} \times \rho_u \times \dot{V}_u \times Y_F \tag{5}$$

The Cantera [3] Python module was used to calculate the different mixture properties. The GRI-Mech3.0 mechanism [9] was used to compute transport properties (*e.g.* dynamic viscosity and thermal conductivity), taking into account the transport properties of each species.

2.2.1 Power and temperatures acquisitions

The electric power generated, P_{TEG}, is estimated using the Ohm law and the parameters U_{cc} and

$R_{e,load}$ using the relation:

$$P_{TEG} = \frac{U_{cc}^2}{R_{e,load}} \tag{6}$$

To estimate the heat absorbed from the flame to the TEG, it was considered that the system is adiabatic, the heat absorbed by the TEG is either converted into electricity or rejected to the HX, where all heat is absorbed by the water. The total heat flow that enters the device (q_{in}) was estimated from:

$$q_{in} = P_{TEG} + \dot{V}_{\mathrm{w}} \times \rho_{\mathrm{w}} \times c_{p_{\mathrm{w}}} \times (T_{\mathrm{w}}^{out} - T_{\mathrm{w}}^{in}) \tag{7}$$

where $\dot{V}_{\mathrm{w}}$ [m^3/s] = [LPM] / (1000 × 60), ρ_{w} [kg/m^3] and $c_{p_{\mathrm{w}}}$ [J/kg K] are, respectively, the volumetric flow rate, density and specific heat capacity of water.

The acquisitions lasted 2 min for each condition. A 5 min interval between conditions was adopted to ensure steady state operation of the system.

2.2.2 PIV

The lens aperture was set to $f/4$, allowing for enough light, reflected from the particles, to enter the camera and the use of small exposure times, which are crucial to avoid the particle motion blur. The camera position was chosen so that the flame holder, the flame and a portion of the flow upstream of combustion could be captured. The images were acquired with a resolution of 32.4 pix/mm (res = 30.86 μm/pix), with a magnification factor M = 4.754. 200 pairs of images were acquired at a rate of 15 Hz. The laser sheet was aligned with the midpoint of the flame holder. As for the chemiluminescence images, the acquisitions were made in a dark environment. The interrogation area (IA) was set to $[\mathrm{IA}_x, \mathrm{IA}_y] = [16,32]$, and the overlap to o_{IA} = 75% in both directions. A time between frames of 75 μs was used. An average correlation method was used to process the 200 pairs of images acquired.

3. Mathematical model

3.1. Finite Element Method

The two-dimensional heat transfer problem can be described by a second order differential equation with a single dependent variable, the temperature T, over the domain Ω with a boundary Γ [6]:

$$-\nabla.\,(\kappa\, \nabla T) = f(x,y) \,\text{in}\, \Omega \tag{8}$$

The terms on the left side of the equation correspond to heat conduction and the terms on the right the heat generation. Following the steps described in [6],

$$[K^e + H^e]\,\{T^e\} = \{f^e\} + \{P^e\} + \{Q^e\} \tag{9}$$

where

$$K_{ij}^e = \int_{\Omega_e} \left(\kappa \frac{\partial \psi_i^e}{\partial x} \frac{\partial \psi_i^e}{\partial x} + \kappa \frac{\partial \psi_i^e}{\partial y} \frac{\partial \psi_i^e}{\partial y} \right) dx\, dy \tag{10}$$

$$F_i^e = \int_{\Omega_e} f \psi_i^e \, dx\, dy + \oint_{\Gamma_e} \hat{q}_n^e \psi_i^e \, ds \equiv f_i^e + Q_i^e \tag{11}$$

$$H_{ij}^e = h^e \oint_{\Gamma_e} \psi_i^e \psi_j^e ds, \quad P_i^e = h^e \oint_{\Gamma_e} \psi_i^e T_\infty ds \tag{12}$$

After creating the matrices and vectors in Equation 9 for all elements of the domain, these were assembled into a single matrix or vector using the correspondence between global and element nodes. Once the global matrix and vectors have been established, and empty lines or columns (all zeros) removed, the system of equations can be solved,

$$\{T^G\} = \left[K^G + H^G\right]^{-1} \{F^G + P^G\} \tag{13}$$

The domain Ω was discretized using linear rectangular elements. Their interpolation functions can be found in [6]

The heat flux vector $\vec{q}$ of each element can be obtained from the temperature derivatives

$$\vec{q} = -\kappa \nabla T = -\kappa \frac{\partial T^e}{\partial x} \vec{x} - \kappa \frac{\partial T^e}{\partial y} \vec{y} \tag{14}$$

One node can be connected to up to four elements, therefore the nodal heat flux components are obtained by averaging the values of the surrounding elements. The difference between the multiple values will decrease with the refinement of the mesh [6].

3.2. TEG governing equations

In any thermoelectric (TE) device, there are two types of materials, one positively charged and another negatively charged, named p-type and n-type, respectively (Figure 4). In the n-type leg, free-electrons carry both charge and heat, while in the p-type leg, this transportation is done by electron-holes. When a temperature gradient is applied to both sides of the device, the charge carriers diffuse from the hot side to the cold side to achieve a new equilibrium state. The concentration of charge carriers increases in the cold side and a positive (negative) potential is built on the cold end of the p-type (n-type) leg [4]. This phenomena is known as the Seebeck effect. When the two legs are joined with the metallic connector, a circuit is formed in which the induced voltage drives the movement of electrons, creating an electrical current.

If an electrical current is applied, heat will be generated or absorbed at the junction between the two semiconductors, thus creating a cooling side and a heating side. This phenomena is termed Peltier effect and allows the thermoelectric to be used as a

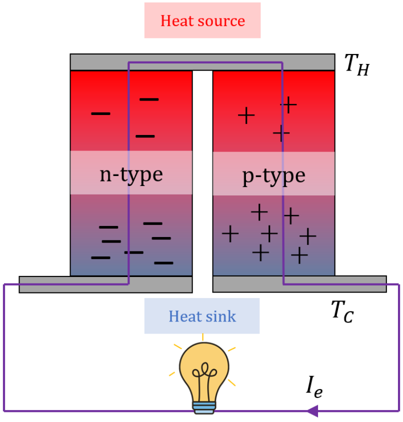

Figure 4: A schematic drawing of a thermoelectric device used for power generation applications.

solid-state heating or cooling device, depending on the direction of the applied current [1].The voltage induced at the thermoelectric terminals is proportional to the difference between the Seebeck coefficient of each leg ($S_p - S_n$), which increases with the thermal gradient in each the leg.

The conversion of heat into electricity with a TEG incorporates different thermoelectric effects in both n and p legs and in the metallic connectors. When a thermal gradient is applied to the TE legs, the flow of electrons or holes from the hot to the cold side causes the build up of an electromotive force proportional to the Seebeck coefficient (S[V/K])(Seebeck effect). When the current I_e flows through the junctions with a discontinuity in Seebeck coefficient, heat $\dot{q}$ is generated or absorbed (Peltier effect). Within the legs, if the current flows in the same/opposite direction of the heat, then, by the Thomson effect, heat is being generated/absorbed in the TE legs. Finally, as in every electrical circuit, when the electrical current flows through the TE legs with electrical conductivity σ, heat is generated (Joule effect).

The energy balance of the aforementioned effects can be written as:

$$\begin{cases} \kappa_p \nabla T_p - \dfrac{\tau_p I_e}{A_{leg}} \left(\dfrac{dT_p}{dx} \right) + \dfrac{I_e^2}{A_{leg}^2 \sigma} = 0 \\ \kappa_n \nabla T_n + \dfrac{\tau_n I_e}{A_{leg}} \left(\dfrac{dT_n}{dx} \right) + \dfrac{I_e^2}{A_{leg}^2 \sigma} = 0 \end{cases} \tag{15}$$

where the terms of the equation correspond to, transport of heat by conduction in the x and y direction, Thomson effect and Joule heating, respectively. The constants κ, τ, σ and S, respectively, thermal conductivity, Thomson coefficient and electrical conductivity, are evaluated at temperature T_p and T_n for the p-type and n-type leg.

Since the heat generated/absorbed due to the Peltier effect occurs at the metallic connectors, their contributions are accounted at the leg ends. For a pair of legs, the heat generated/absorbed at its ends can be calculated from:

$$\begin{cases} q''_{Peltier,x=-L} = \dfrac{-I(S_p^{T_h} - S_n^{T_h})\, T_h}{2\, A_{leg}} \\ q''_{Peltier,x=L} = \dfrac{I(S_p^{T_c} - S_n^{T_c})\, T_c}{2\, A_{leg}} \end{cases} \tag{16}$$

where the superscript T denotes the temperature at which S is evaluated and L is the half length of the leg ($L = 1.9$ mm for the TEG used). T_h and T_c represent the temperatures at the hot side and cold side of the legs, right after/before the ceramic plates (Figure 5).

The TEG legs are electrically connected in series (Figure 5) and arranged in a matrix structure. Each row i contains N_i pair os legs. For the TEG module used in this work, each row contains 5 pairs of legs, except the top and bottom rows which have one leg less. The voltage built up at the TEG terminals, U_{oc}, can be calculated from:

$$U_{oc} = \sum_{i=1}^{10} N_i \int_{T_c}^{T_h} \left[S_p(T_p) - S_n(T_n) \right] dT \tag{17}$$

The TEG internal electrical resistance, $R_{e,TEG}$ was calculated from the leg materials electrical properties and the aluminium cables (diameter $d_{cable} = 0.6$ mm, length $L_{cable} = 11$ mm) welded to the TEG terminals.

$$R_{e,TEG} = \sum_{i=1}^{10} \frac{N_i}{A_{leg}} \int_{-L}^{L} \left[\frac{1}{\sigma_n^{Tp}} + \frac{1}{\sigma_n^{Tn}} \right] dx + 2 \frac{L_{cable}}{A_{cable}\, \sigma_{Al}} \tag{18}$$

From the voltage induced at the TEG terminals and the resistances, the current I_e can be calculated:

$$I_e = \frac{U_{oc}}{R_{e,TEG} + R_{e,load}} \tag{19}$$

The electrical power generated, P_{TEG} can finally be calculated from its electrical analog

$$P_{TEG} = I_e^2 \, R_{e,load} \tag{20}$$

Since the thermodynamic circuit was evaluated in two dimensions and the electrical circuit symplified to one dimension, the difference between heat flows q_H and q_C is not equal to P_{TEG}.

The thermoelectric properties (κ, σ and S) and the heat generation/absorption terms require information about the temperature distribution along the leg to be computed. Therefore, an iterative routine was implemented to solve the system. On the first iteration, it is assumed a constant value for k

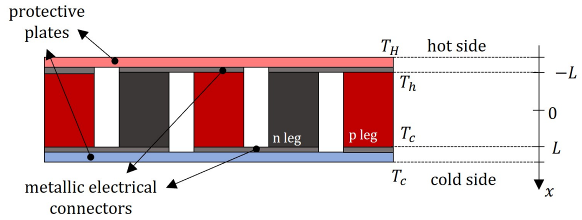

Figure 5: Schematic view of one row of the TEG

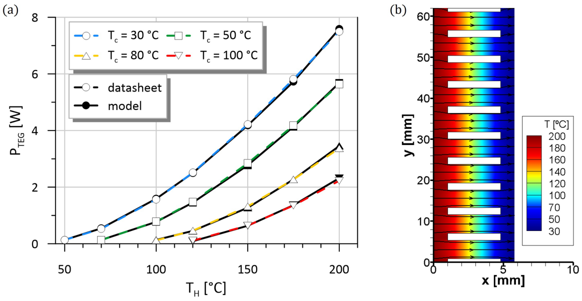

Figure 6: (a) Variation of P_{TEG} with T_H and T_C surface temperatures; dashed lines with unfilled markers denote the reference values from the TEG datasheet whilst solid black lines with filled markers the results obtained with the mathematical model (b) temperature distribution and streamlines across the TEG with T_H = 200 °C and T_C = 30 °C

along the TEG legs and the thermoelectric effects are not considered. In the following iterations, the thermoelectric properties are calculated with the temperature distribution of the previous iteration. If the relative difference of I_e and $R_{e,TEG}$ between successive iterations was smaller than 10^{-4}, the iterative process stops and the model returns the desired outputs.

3.3. Boundary Conditions

3.3.1 Essential boundary conditions

The TEG surface temperatures, T_H and T_C, were used to solve the system of equations and to estimate the thermal conductivity of the ceramic protective plates of the TEG. The temperatures $T_H = 200$°C and $T_C = 30$°C were used as boundary conditions and the thermal conductivity was modified until P_{TEG} equals the value from the TEG datasheet. The final result was a thermal conductivity equal to $\kappa = 3.675$ [W/mK].

To validate the model for other conditions, the power generated was calculated with the TEG with $R_{e,load} = R_{e,TEG}$ and different combinations of temperatures T_H and T_C as boundary conditions. The obtained results were compared with the values in the datasheet, an average difference of 0.03 W was observed. This overlap between the model and the datasheet can be observed in Figure 6a. The temperature distribution and streamlines across the TEG with T_H = 200 °C and T_C = 30 °C are illustrated in Figure 6b. The streamlines are obtained from the heat flux vectors (Equation 14).

3.3.2 Natural boundary conditions

The heat flux from the flame and burnt gases to the wall is characterized by peak heat flux in the region of flame quenching, transported by conduction, followed by convective heat transfer of the hot gases. Westbrook *et al.* [10] suggested that a CH_4 + Air premixed flame in quenching extinguishes as the flame temperature approaches $T_{flm} \approx 1500$K. The fraction of the total heat that is transferred in quenching can, thus, be estimated from d_q, the TEG temperatures and q_{in}:

$$\frac{q_q}{q_{in}} = \frac{\kappa_u/d_q(T_{flm} - T_H) \times l_s \times \delta_{flm}}{q_{in}} \tag{21}$$

Given that this fraction is close to 1%, the conduction contributions can be neglected.

The convective heat flux between burnt gases and the wall can be calculated from:

$$q''_{conv}(y') = h_{y'}\,(T_{brt} - T_{wall}) \tag{22}$$

where $h_{y'}$ represents the convective heat transfer coefficient at a distance y' from the leading edge ($y' = 0$). T_{brt} and T_{wall} denote the temperatures of the burnt gases and at the wall surface. Given the magnitude of velocities of the flow and the small area where heat transfer occurs, the temperature of the burnt gases can be assumed to be equal to the adiabatic flame temperature $T_{flm,ad}$.

The Nusselt number Nu can be written as a function of h_y or described as a function of the Reynolds and Prandtl number Pr:

$$Nu = \frac{h_{y'}\,y'}{\kappa} = a\,Re_{y'}^{1-b} Pr^{1/3} \tag{23}$$

That correspond to a hydrodynamic boundary layer described as:

$$\delta = c\,y'\,Re_{y'}^{-b} \tag{24}$$

where δ corresponds to the height of the boundary layer.

Although there is not a reference velocity to correctly define the boundary layer, it is possible to describe the development of a hypotetical boundary layer by tracing isolines with a specific V. Figure 7a presents the velocity contours and isolines for a BG100 flame with $Re = 300$ and $\phi = 0.7$ interacting with the GS wall. The points of the isoline with $V = 1.9$m/s (Figure 7b) with $23\,mm < y < 38\,mm$

($y' = y - 23$) were adjusted to the Equation 24 to obtain the value of the constant b. A value of $b = 0.667$ and $b = 0.652$ were obtained with an uncertainty of $u_\sigma < 0.006$ for the GS and the clay wall. Different flame conditions may cause small variations in the value of b, but since its influence on the overall heat flux is very small, a constant value of b was assumed for all conditions.

The constant a of Equation 23 was estimated by minimizing the mean squared error between the experimentally obtained P_{TEG} and the results calculated with the model. To reduce computational time, the error function was minimized for results of BG80 flames, instead of the results from the different fuel blends. To obtain the area for heat transfer, results from OH* chemiluminescence with the GS wall were used to obtain the flame height.

The gas properties (κ, Pr and υ) were evaluated at the average between flame and wall temperatures $T = (T_{flm,ad} + T_{wall})/2$. The fluid properties were the result of a 1D freely propagating flame simulation using the Cantera [3] Python module, with GRI-Mech3.0 [9] mechanism to compute the transport properties.

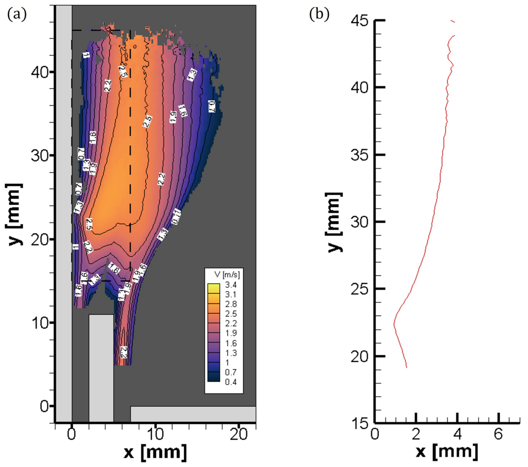

Figure 7: (a) Velocity magnitude for BG100 flame with $\phi = 0.7$ and $Re = 300$ interacting with the GS wall and (b) isoline where $V = 1.9$m/s.

4. Results

To evaluate the performance of the TEG, tests were realized for all fuel blends, Re and ϕ. As equivalence ratios approach stoichiometry, the increase in the flame speed led to resonating flames at higher Re ($Re = 300$ and $Re = 350$). On the other hand, for certain fuels, for lower Reynolds ($Re = 100$ and $Re = 150$) flame flashback occurred. In the setup used (flame in SWQ), the flame flashback is characterized by the flame branch further away from the wall (Figure 1b) to burn upside down, *i.e.* from the base of the burner up to the flame holder. Conditions where flame flashback occurred were not evaluated.

Clay wall

For a fixed Re, P_{TEG} increased significantly with the increase of ϕ. On the other hand, increasing Re had a negligible effect on P_{TEG}, for a fixed ϕ. The temperature difference between both sides of the TEG (T_H - T_C) also increased with ϕ. Higher ΔT yields larger voltage drops at the TEG terminals (Seebeck effect), which results in the increase of P_{TEG}. An example of the influence of work conditions is presented in Figure 8(a) for BG80 flames, P_{TEG} is represented by solid lines with different colours and markers, depending on the equivalence ratio.

The thermoelectric efficiency η_{TEG} was estimated from the total heat that enters the module q_{in} and the electrical power generated P_{TEG}:

$$\eta_{TEG} = \frac{P_{TEG}}{q_{in}} \tag{25}$$

In ideal conditions (adiabatic system and matched load resistance, $R_{e,load} = R_{e,TEG}$), η_{TEG} can be described as function of the thermoelectric figure of merit $Z\overline{T}$ and surface temperatures [7]:

$$\eta_{TEG} = \left(1 - \frac{T_C}{T_H}\right) \frac{\sqrt{1 + Z\overline{T}} - 1}{\sqrt{1 + Z\overline{T}} + \dfrac{T_C}{T_H}} \tag{26}$$

The flame conditions had the same impact on η_{TEG} as for P_{TEG} and ranged from 1.80% to 2.76% for all fuels and flame conditions. The minimum was observed for BG60 with $Re = 150$ and $\phi = 0.7$ and the maximum for BG80 with $Re = 300$ and $\phi = 1.0$.

Since T_C fluctuates at most 5 °C between work conditions, the fluctuations of P_{TEG} and η_{TEG} (from Eq. 26) will depend almost entirely of the oscillations of T_H. For this reason, the maximum power and TEG efficiency, in each fuel blend, were attained for the highest ϕ tested.

The global system efficiency was estimated from the flame power P_{flm} and P_{TEG}:

$$\eta_{glob} = \frac{P_{TEG}}{P_{flm}} \tag{27}$$

For a fixed ϕ, η_{glob} decreases rapidly with the increase of Re, as shown in Figure 8(a) by the dotted lines, with different colours and markers depending on ϕ, for BG80. For all fuels and conditions η_{glob} ranged from 0.17% to 0.39%. Since η_{HT} is almost insensitive to changes in the Reynolds, the system efficiency losses with increasing Re must relate with

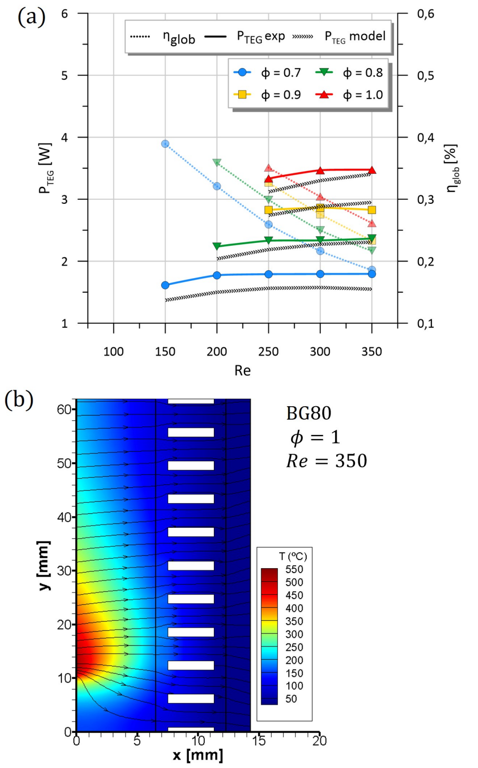

Figure 8: (a) Map of P_{TEG} and η_{glob} for BG80 flames with the clay wall; continuous lines link experimental P_{TEG} whilst dotted lines correspond to η_{glob}; black lines denote the values obtained with the mathematical model (b) temperature distribution and streamlines for BG80 with $\phi = 1$ and $Re = 350$.

the heat transfer efficiency η_{HT}:

$$\eta_{HT} = \frac{q_{in}}{P_{flm}} \tag{28}$$

For the work conditions studied, η_{HT} ranged from 8.66% to 19.69%, the lowest values attained for high Re. For BG80, the lowest η_{HT} was 8.93%, obtained for $\phi = 0.7$ and $Re = 350$ while the highest was 19.69%, obtained for $\phi = 0.7$ and $Re = 200$. For a fixed Re, small gains in η_{HT} were observed when increasing ϕ, which may be attributed to the small increase of the n and p-type legs thermal conductivity. Since the fluctuations of η_{HT} are larger than the ones of η_{TEG}, the heat transfer efficiency is the dominant factor in the system's efficiency. The tendencies of P_{TEG} and efficiencies with the work conditions were observed for all fuel blends tested.

The estimations of P_{TEG} obtained with the mathematical model developed in this work (section 3) are presented in Figure 8a through the black lines. The values predicted by the model were very similar to the experimental results, with an average difference of 0.16 W for all fuels and flame conditions. The low thermal conductivity of clay causes the heat to flow essentially in the x direction as is illustrated by the streamlines in Figure 8b. This is then reflected on the temperature distribution upstream of flame quenching (at *ca.* $y = 10.5$ mm for BG80, $\phi = 1$ and $Re = 350$), which are significantly lower than the temperatures downstream $(y < 10mm)$.

Diluting BG100 (CH_4) with CO_2, in a 80/20 and 60/40 proportion, had a similar impact on P_{TEG} and η_{glob} as the reduction of equivalence ratio. In both cases, the decrease of combustible fuel causes the loss of flame and burnt gas temperatures, and lower heat release rate, which generates lower TEG surface temperatures. Adding 20% of CO_2 to BG100 causes an average power reduction of 0.11 W (±0.026 W, 1σ-standard deviation). Adding other 20% to what is now BG80 causes power losses in the range of 0.17 W $< \Delta P_{TEG} <$ 0.67 W. The largest differences occur at stoichiometric equivalence ratios. Blending H_2 to the BG mixtures mitigates the electrical power losses caused by CO_2 dilution.

Influence of wall material

The equivalence ratio has the same impact on P_{TEG} with the GS wall as previously described with the clay wall. However, the increase of Re resulted in small increments of P_{TEG}, becoming less pronounced for $\phi = 0.7$ and high Reynolds numbers. The trends observed with the GS wall, in regard to flame work conditions, are in accordance with the results from Santos *et al.* [8] with an aluminium wall. The influence of flame conditions on P_{TEG} and η_{glob} with the GS wall are illustrated in Figure 9(a) for BG80 flames. The P_{TEG} fluctuations due to flame conditions were also reflected by the mathematical model (black lines in Figure 9(a)). The values of P_{TEG} obtained with the mathematical model deviated, on average, 0.14 W from the value measured experimentally.

The high κ_{wall} of the GS wall ($\kappa_{wall} = 56.7$ [W/mK]) allows the intense heat flux from flame quenching to dissipate downstream, as illustrated through the streamlines of the heat flux obtained with the mathematical model (Figure 9b). Overall, the power generated with the GS wall is higher than the achieved with the clay wall, with the same fuel and work conditions. The difference in P_{TEG} between GS and clay, ΔP_{TEG}, increased with equivalence ratio and Re. For $\phi = 0.7$, ΔP_{TEG} is the smallest, *ca.* 0.2 W. The maximum ΔP_{TEG} was 1.02 W, observed for BG80 with $\phi = 1.0$ and $Re = 350$. The higher κ_{wall} and smaller thickness of the GS wall, compared to the clay wall, lead to an increase of the heat transfer efficiency, $0.69\% < \Delta\eta_{HT} < 4.27\%$. Higher temperatures on

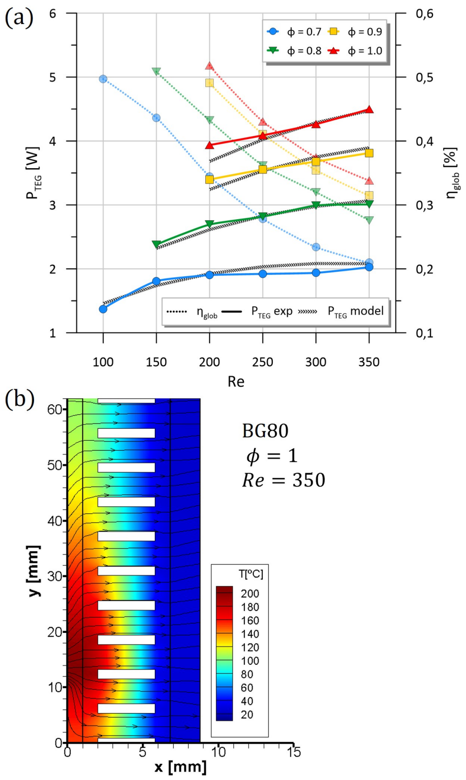

Figure 9: (a) Map of P_{TEG} and η_{glob} for BG80 flames with the GS wall; continuous lines link experimental P_{TEG} whilst dotted lines correspond to η_{glob}; black lines denote the values obtained with the mathematical model (b) temperature distribution and streamlines for BG80 with $\phi = 1$ and $Re = 350$.

the TEG hot surface resulted in higher thermoelectric efficiency, with $\Delta\eta_{TEG}$ up to 0.31%, and global efficiency, with improvements up to $\Delta\eta_{glob}$ 0.09% ($\Delta\eta_i = \eta_i(GS) - \eta_i(clay)$).

With respect to the influence of fuel blends in the electrical power output with the GS wall, the same trends were observed, adding CO_2 causes a reduction of P_{TEG} which are compensated when H_2 is blended.

Compared to the GS wall, the clay wall has a much lower thermal conductivity and larger thickness, and therefore a higher thermal resistance, which should make a good thermal insulator and achieve lower temperatures on the hot surface of the TEG. However, the temperatures obtained for both walls with the lowest thermocouple (positioned at $y = 16$ mm from the bottom of the TEG) were very similar, always smaller than 15 °C. With the increase of ϕ, temperatures in the top part of the TEG (obtained with the thermocouple positioned at $y = 16$ mm from the top of the TEG), where heat transfer is dominated by convection, exhibit a larger difference, up to 30 °C.

The small κ_{wall}(clay) makes heat flow through the wall almost unidirectional (Figure 8b), with negligible vertical heat dissipation, which means that the largest differences (compared to GS) in temperature should occur upstream of the quenching zone. This hypothesis was verified by analysing the temperature profiles at the hot side of the TEG obtained from the model with both walls (Figure 10). The power losses between the two materials may be attributed to this difference.

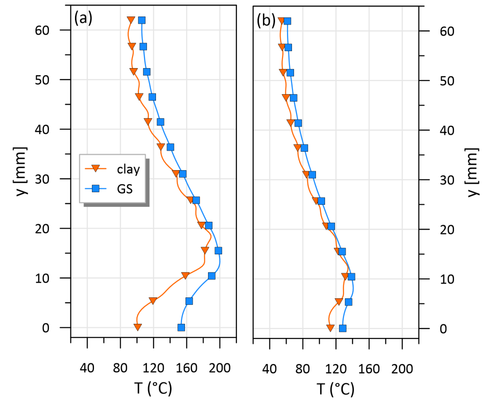

Figure 10: Temperature profiles for BG80 with (a) $\phi = 1.0$ and $Re = 350$, and (b) $\phi = 0.7$ and $Re = 150$

To better understand the contribution of wall material, flame conditions and fuel blend to the power generated, we attempted to relate P_{TEG} with the wall's thermal conductivity (κ_{wall} [W/mk]) and thickness (t_{wall} [m]), Reynolds number and flame temperature ($T_{flm,ad}$ [K]), which varies linearly with ϕ from 0.7 to 0.9 for BG100 flames [?] and encompasses the effects of adding CO_2 and H_2, with the equation:

$$P_{TEG} = k\, r_{wall}^{a}\, T_{flm}^{b}\, Re^{c} \tag{29}$$

where $r_{wall} = t_{wall}/\kappa_{wall}$ represents the thermal resistance per unit area. In addition to the results obtained in this work, values of P_{TEG} obtained with an aluminium wall (90 × 75 × 1 mm) presented by [8] were also incorporated. The parameters a, b, c and k were determined by finding the minimum the mean squared error of the error function:

$$F(k,\, a,\, b,\, c) = \left| P_{TEG} - k\, r_{wall}^{a}\, T_{flm}^{b}\, Re^{c} \right| \tag{30}$$

The final correlation is presented in Figure 11. The equation obtained shows good agreement with the experimental values for all materials, fuels and flame work conditions. The obtained exponents indicate that:(i) T_{flm} is the dominant factor on P_{TEG} and, since b = 3.79 >1, for successive increments of T_{flm}, the gains on power yielded will increase; (ii) since c = 0.342 <1, the gains of P_{TEG} obtained by increasing Re will decrease, until a point where the effects of Re are no longer noticed; (iii) since a = -0.0363 <0, for a fixed wall thickness and successive increments of κ_{wall}, the gains on power generated will decrease.

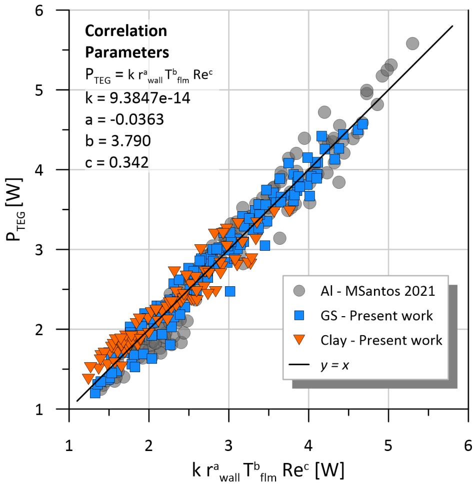

Figure 11: Correlation of P_{TEG} using an equation of the type $P_{TEG} = kr^a_{wall}T^b_{flm}Re^c$

.

5. Conclusions

The main objective of this work was to evaluate the potential use of clay as a wall material in the direct heat-to-electricity power conversion using a thermoelectric generator. The influence of wall material to the system performance (TEG output power and efficiency) and to the flame wall interaction (d_q, heat release rate and velocity field) was studied. A mathematical model was developed, based on the finite element method, to complement the analysis of the contribution of the wall (thermal conductivity and thickness) to the electrical power generated.

Walls made of clay and GS were tested. The results with the GS wall were used as reference, when comparing with the clay wall. Each wall was studied with seven fuel blends. BG100 and two biogas mixtures (BG80 and BG60), to which H_2 was added in small quantities (up to 20%), were selected. Each fuel blends was studied with a range of equivalence ratios (from 0.7 to 1.0) and burner Reynolds number (from 100 to 350). Velocity fields were investigated using PIV techniques.

The main findings of the present work are:

1. P_{TEG} and η_{TEG} increase significantly with ϕ, regardless of the wall material. Changes in Re cause variations of P_{TEG} with the GS wall, but not with the clay one. The increase of Re causes large drops in η_{glob}. The difference in P_{TEG} between wall materials increases with flame temperature.
2. The decrease in gases density in the flame front causes streamlines to deviate away from the wall right after the quenching region. Higher temperatures at the clay surface decreases gases density in the vicinity of the wall, resulting in higher velocities.
3. The mathematical model developed showed an excellent agreement with the experimental results, with an average error under 7%.

Acknowledgements

The author would like to thank Professor Edgar Fernandes and PhD Sandra Dias for all the supervision and guidance throughout the development of this work.

References

[1] *Thermoelectrics Handbook*. CRC Press, 2006.

[2] Dantec Dynamics. *DynamicStudio User's Guide*. Skovlunde, 2016.

[3] H. K. M. David G. Goodwin, Raymond L. Speth and B. W. Weber.

[4] M. Hamid Elsheikh, D. A. Shnawah, M. F. M. Sabri, S. B. M. Said, M. Haji Hassan, M. B. Ali Bashir, and M. Mohamad. A review on thermoelectric renewable energy: Principle parameters that affect their performance. *Renewable and Sustainable Energy Reviews*, 30:337–355, 2014.

[5] F. P. Incropera and D. P. DeWitt. *Fundamentals of Heat and Mass Transfer*. John Wiley & Sons, Inc., 7th edition edition, 2011.

[6] D. J. N. Reddy. *n Introduction to the Finite Element Method*. McGraw-Hill Education, 3rd edition edition, 2005.

[7] G. Min and D. M. Rowe. Conversion efficiency of thermoelectric combustion systems. *Energy Conversion, IEEE Transactions on*, 22:528 – 534, 07 2007.

[8] M. D. Santos, S. I. Dias, A. P. Gonçalves, and E. C. Fernandes. Thermoelectric power generation from biogas+h2 flames: Influence of flame-wall interaction. *Experimental Thermal and Fluid Science*, 126:110350, 2021.

[9] G. P. Smith, D. M. Golden, M. Frenklach, N. W. Moriarty, B. Eiteneer, M. Goldenberg, C. T. Bowman, R. K. Hanson, S. Song, J. William C. Gardiner, V. V. Lissianski, , and Z. Qin.

[10] C. K. Westbrook, A. A. Adamczyk, and G. A. Lavoie. A numerical study of laminar flame wall quenching. *Combustion and Flame*, 40:81–99, 1981.